

Evolution of Ripple Field Architecture during Sediment Transport, as Measured by CT Scanning

Long Bernard and Montreuil Stéphane
*Centre Eau Terre Environnement
Institut national de la recherche scientifique
Université du Québec
Canada*

1. Introduction

Despite the advent of ever more sophisticated technologies, the study of sediment transport remains highly relevant. Ongoing climate change adds urgency to the need to understand phenomena governing sediment transport. During sediment movement, the architecture of the sediment bed evolves (Nummedal et al., 1993; Allen and Posamentier, 1994; Van Wagoner, 1995). This chapter focuses on the fundamental processes involved in sediment transport and aims to define and characterize the evolution of the water-sediment mixture in a migrating sand ripple field under a stationary flow regime, from the flow surface to the base of the sediment bed. In an experimental sediment flume with attached computed tomography (CT)-scanner, the sediment density of a ripple field was studied at different phases of its architectural evolution using three- and four-dimensional X-ray scanning, under several flow regimes and with different grain sizes. This approach yielded a detailed understanding of the parameters involved in transport of sand-grade sediment.

2. Methods

This study used two hydraulic flumes. One was a vertical, closed-loop flume 3048 mm long and 1219 mm high designed by Teeter and Pankow (1989). The inner rectangular section of the flume (152 mm by 304 mm) passed through the mobile gantry of a computed tomography (CT)-scanner. The lower part of the tunnel was partly filled with a 30 mm-thick layer of C-109 Ottawa sand (0.37 mm grain size, with bulk dry density of $1.56 \text{ g}\cdot\text{cm}^{-3}$). The flow regime was adjusted by an electrical motor to $25 \text{ cm}\cdot\text{s}^{-1}$ and controlled by a Doppler flow meter (Controlotron 1010N). For more details of this apparatus, see Montreuil (2006). In this flume experiment, the volume element (voxel) chosen was 0.39 mm by 0.60 mm by 1.00 mm. Typical density profiles along the ripple bed were extracted from the CT-scanner measurement matrix of $512 \times 512 \times 512$ voxels and a $305 \times 305 \times 200$ mm volume. The second flume was an open acrylic flume ($300 \times 300 \times 7000$ mm) looped by a pump with $1.51 \text{ m}^3\cdot\text{min}^{-1}$ capacity. The rectangular section of the flume (300×300 mm), passed through the mobile gantry of the CT-scanner (Fig. 1). The steady flow, measured by a Controlotron

1010 Doppler flow meter, was controlled by a PID regulator using a pneumatic valve installed in the pump looping circuit. Three flow velocities and two grain sizes were used to confirm the existence of several points and zones and to identify their respective locations over a ripple. To create a natural sand column, the flume base was sand-blasted, as recommended by Madsen and Durham (2007), and was filled with a 50 mm-thick sand layer. The CT-scanner was able to accommodate a large open-channel flume scanner (300 x 300 x 7000 mm; Fig. 2) and allowed continuous measurement of both suspended and bedload sediment, without hydraulic interference on the water or sediment, for the 512 x 512 x 1500 mm voxel matrix. In the open-flume experiment, the voxel dimensions were 0.6 x 0.6 x 0.6 mm.



Fig. 1. CT-scanner gantry moving along the flume on four parallel rails and open-channel flume fixed on the examination table.

The CT-scanner imagery corresponds to a 3D linear X-ray attenuation voxel image (Fig. 2). The instantaneous slice group measured forms a volumetric 3D matrix (Fig. 3). X-ray attenuation is a function of the material density, its effective atomic number, and the analyzed sample thickness. Although Dului (1999) indicated that four effects characterize X-ray interaction with a material, medical CT-scanners, which use energy below 150 keV, exhibit only two of these effects: the photoelectric and Compton effects. In this type of study, the photoelectric effect dominates (Moore, 2004).

In this study, two different techniques were used to undertake pseudo-instantaneous measurement (Lagrangian) and time-evolution measurement (Eulerian). The global volume technique (GVT) uses the CT-scanner to measure a large volume, giving a picture at a specific moment (Lagrangian) (Fig. 2). This technique, used by Montreuil (2006) and Montreuil and Long (2007), gives a 3D image of the entire sand ripple with a maximum available length of 1500 mm. The global volume technique is useful in comparing all densimetric profiles over a sand ripple within 90 s for a 1500 mm-long bedform. To measure an entire ripple, the CT-scanner needs to move along the flume. The simultaneous motion of the CT-scanner gantry and the fluid inside the flume reveals an uncertainty due to moving

sediment during X-ray integration. The global single-volume technique is, therefore, a pseudo-instantaneous measurement technique.

The second technique, the periodic single volume technique (PSVT), provides an Eulerian representation of the internal bedload architecture constancy during sand ripple migration.



Fig. 2. Three-dimensional X-ray image of a sediment bed 300 mm wide by 300 mm high by 900 mm long, formed from 1500 slices of 512 x 512 pixels.

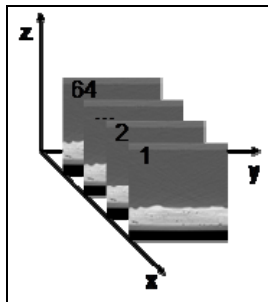


Fig. 3. CT-scanner measurement volume formed from 64 slices 0.6 mm thick at 0.6 mm intervals. Each slice has a resolution of 512 x 512 pixels and the set forms a volume of 300 x 300 x 18 mm.

To perform this measurement, a volume formed from thirty slices (each 300 x 300 x 0.6 mm) was measured, keeping the same flume position (i.e., the CT-scanner gantry remained immobile). The volume, including the sand ripple bed and the water column, was measured instantaneously by the 64 CT-scanner line of sensors. Each volume was measured with a time-space Δt sample in seconds or minutes depending on ripple migration velocity, yielding the density of the ripple moving across a spatially fixed volume (Fig. 4).

The flume axes were defined as follows: x for the flow direction, y for the horizontal cross-section, and z for the flume height (including both sediment and water column).

Various other methods have been used to measure bedform propagation, including stereophotogrammetry (Sternberg, 1967), direct measurement (Langhorne, 1981), high-resolution echo-sounding (McLean, 1983), and ripple-shadowing (Wilkinson et al., 1985).

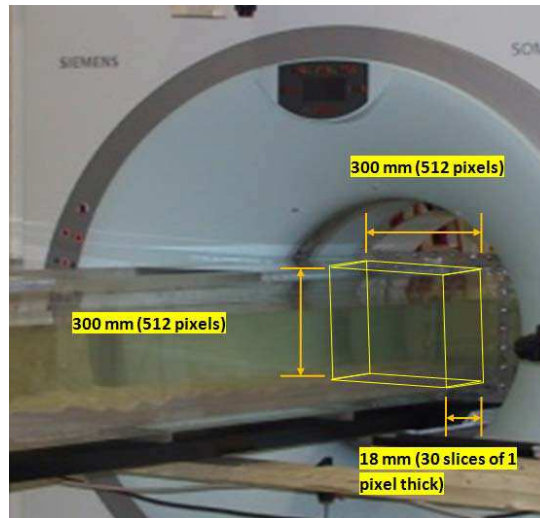


Fig. 4. Acrylic flume passing through the immobile CT-scanner gantry yielding a measurement volume of 300 x 300 x 18 mm.

Medical CT-scanners can be used to measure relative density of materials such as sand layers in sedimentological studies (Duliu, 1999; Ketcham and Carlson, 2001; Mees et al., 2003; Duchesne et al., 2006). Relative density values measured vary from -1024 to +3071 Hounsfield units (HU; Kak and Slaney, 1999). Air and water values are -1000 HU and 0 HU, respectively (Ketcham and Carlson, 2001). The quartz sand used has a density similar to that of human bone (1477 HU) and spinal core (1609 HU; Schneider et al., 1996). Density measurements were converted to $\text{g}\cdot\text{cm}^{-3}$. The following equation was used to convert and correct the beam-hardening and Beer's law effects of X-ray measurements (ASTM, 1992):

$$\rho_s = 0,0257 \left(\frac{\text{HU} + 1024}{1000} \right)^2 + 1,0209 \left(\frac{\text{HU} + 1024}{1000} \right) - 0,0254 \quad (1)$$

where ρ_s is the density of the fluid-sediment mixture inside the flume and HU is the relative density measured by the CT-scanner.

To validate the confidence level of the data, a standard deviation was calculated for each section of the ripple using a group of profiles. The results indicate a standard deviation of $0.018 \text{ g}\cdot\text{cm}^{-3}$ for the water column, which reflects turbulence and Brownian motion (Brown, 1828) for zero-velocity measurement. For the suspended-transport zone, the standard deviation of $0.022 \text{ g}\cdot\text{cm}^{-3}$ is due to the turbulence, bed proximity, and heterogeneous concentration of suspended sediment. At the interface between suspended load and the upper bedload transport zone, the standard deviation reaches a maximum of $0.023 \text{ g}\cdot\text{cm}^{-3}$. This high value indicates the presence of air bubbles trapped in the sand and a difference in the degree of compaction between the different laminations.

For the water column, the concentration of sediment in water was calculated using the Bridge and Demicco (2008) equation,

$$C = \frac{\rho_s - \rho}{\rho_{mix} - \rho} \tag{2}$$

where ρ_{mix} is the density of the sediment-water mixture, ρ_s is the sediment density, and ρ is the water density at the experimentation temperature.

The suspended load, located between the reattachment point and the separation point, is calculated using dynamic viscosity profiles defined in the Bridge and Demicco (2008) equation:

$$\mu_s = \mu(1 + 2.5C + 6.25C^2 + 15.26C^3) \tag{3}$$

where μ is the pure fluid viscosity and C is the sediment concentration.

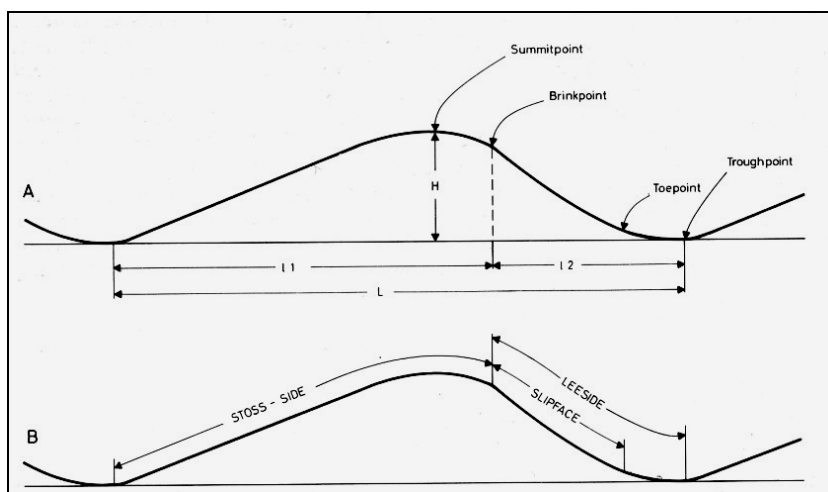


Fig. 5. Definition of sand ripple “sections,” after Reineck and Singh (1975). (A) Sand ripple form is defined by a succession of deterministic points. (B) Sand ripple is divided into erosional and depositional zones.

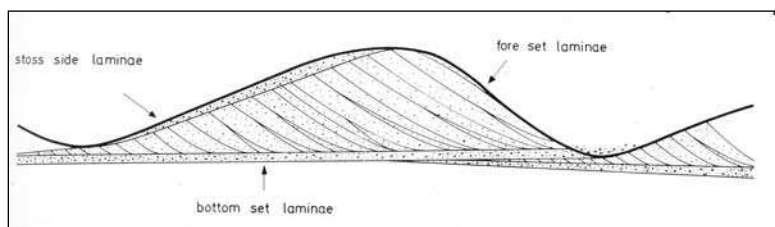


Fig. 6. Definition of sand ripple “sections,” after Reineck and Singh (1975). The internal structure of the sand ripple consists of three lamina sets.

This study used the sedimentological definitions of Reineck and Singh (1975; Figs. 5 and 6). Ripple zones are detailed in Figure 7. Reineck and Singh (1975) defined sediment

parameters by delineating and naming distinct zones and points in the formation of a sand ripple. Values for parameters were assigned based on measurable or observable attributes at a given time. Ripple “zones” are defined perpendicular to layering, whereas the ripple “section” is defined according to horizontal location.

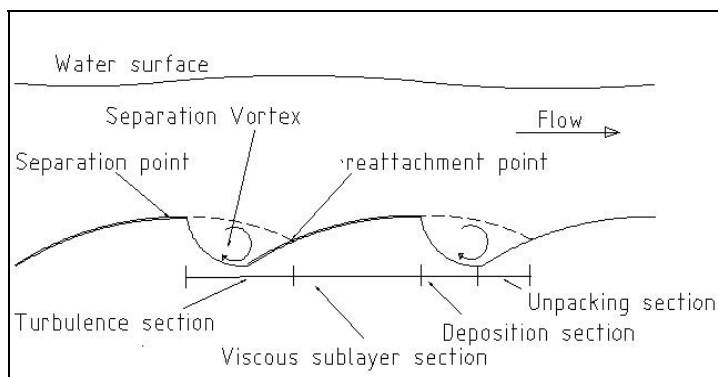


Fig. 7. Definition of sand ripple “sections”: turbulent section (contains vortices), viscous sublayer section (also called the pure transport section), depositional section, and, within the turbulent section, a sediment unpacking section (also called the erosion section). Adapted from Bridge and Demicco (2008) and based on Bennett and Best (1995).

Montreuil and Long (2007) emphasized the presence of a maximum point, at which the density along the ripple reaches a maximum value. A ripple grows by deposition of successive foreset laminae that avalanche down the lee side of the ripple. Foreset laminae are constantly being eroded on the stoss side of each ripple during ripple migration; some of this remobilized sediment moves by bedload and defines stoss-side laminae that are nearly perpendicular to the foreset laminae. Reineck and Singh (1975) identified a static foreset lamina field that is constantly eroded and stoss-side laminae which consist of sediment in continuous motion.

Other definitions, including crest and trough concepts, are from Tucker (2001) and Bridge and Demicco (2008), who described the formation of current ripples (Figs. 7 and 8). The formulation of fluvial-type processes in a flume (Yalin, 1992) and the sediment transport mechanics associated with current ripples (Yalin, 1977) have been clearly stated and are the foundation for the definitions in this study. Kastaschuk and Villard (2001) proposed a conceptual model for suspended load flow, in which the internal boundary layer meets the viscous sublayer and the wake region is not characterized by vortical activity. Middleton and Southard (1977) proposed a schematic definition of shear stress and pressure relative to the flow velocity profile and profile position. Finally, Allen (1968, 1984) provided a general picture of sandy sediment-depositional systems that is the starting point of this work.

In general, the internal geometry of a ripple is a consequence of the forces acting at the beginning on stationary and moving fluids, and corresponds to the relationship between velocity and pressure in a moving fluid, as described by the Bernoulli equation. Flow over a ripple field, however, is not laminar, but turbulent. The transition between laminar shear flow and turbulent shear flow is produced by turbulent eddies. Such eddies are critical to bedform formation and evolution. Turbulent shear flow is due to the addition of a viscous shear stress like that defined in the Reynolds equation.

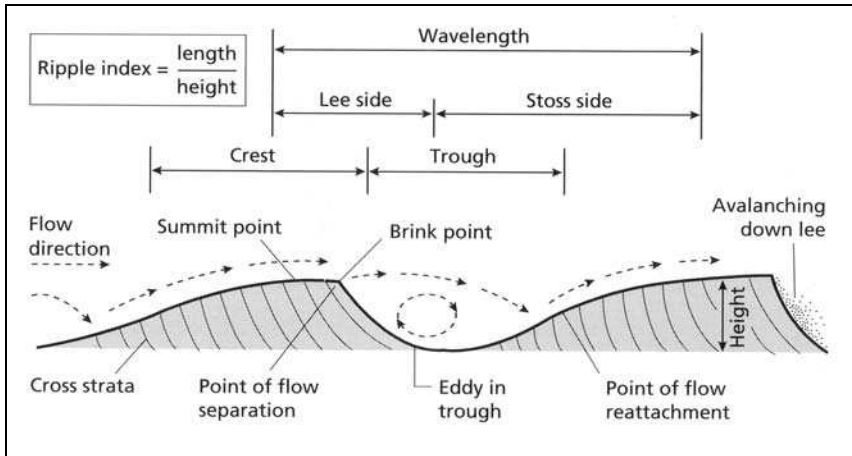


Fig. 8. Complementary general sand ripple definition, after Tucker (2001).

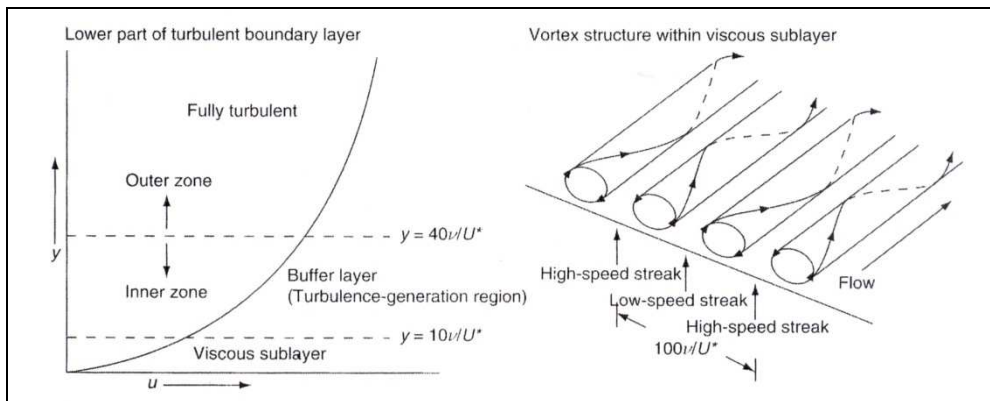


Fig. 9. Main structural features of turbulent boundary layers (after Bridge and Demicco, 2008, and modified from Bridge, 2003).

The turbulent boundary layer in steady, uniform, turbulent flow is a function of bottom friction. Friction at the solid boundary of the water flow (Fig. 9) causes a reduction in flow velocity near the boundary. The main structural features of the turbulent boundary layer define three zones (Bridge, 2003). Very close to the sediment is a viscous sublayer a few millimeters thick. This basal layer is overlain by a buffer zone called the inner zone, which consists of a turbulence-generating region. The uppermost layer is the full-turbulence zone, which is referred to as the outer zone. The boundary between the viscous sublayer and the inner zone is defined by

$$\delta y = \frac{10\nu}{U_*} \tag{4}$$

The boundary between the two turbulent zones is defined by

$$\delta y = 40 \nu / U_* \quad (5)$$

where ν is the kinematic viscosity and U_* is the shear velocity, defined as

$$U_* = \sqrt{(\tau_0 / \rho)} \quad (6)$$

where τ_0 is the mean fluid shear stress at the bed and ρ is the fluid density.

The three zones are not uniformly distributed above the ripple bed during sediment transport because U_* is not constant. The present work illustrates this variation empirically.

3. Definitions

3.1 Three-dimensional sedimentological architecture of a sand ripple field

Density profiles were examined using the classical approach of separating and isolating the suspended load from the bedload, as done by Carmenen and Larson (2004). The density profiles provided by the 3D matrix were analyzed continuously from the water surface to the bedload base. A typical density profile (Fig. 10) depicts transport zones that are delimited by characteristic density points. More details are available in Montreuil and Long (2011b).

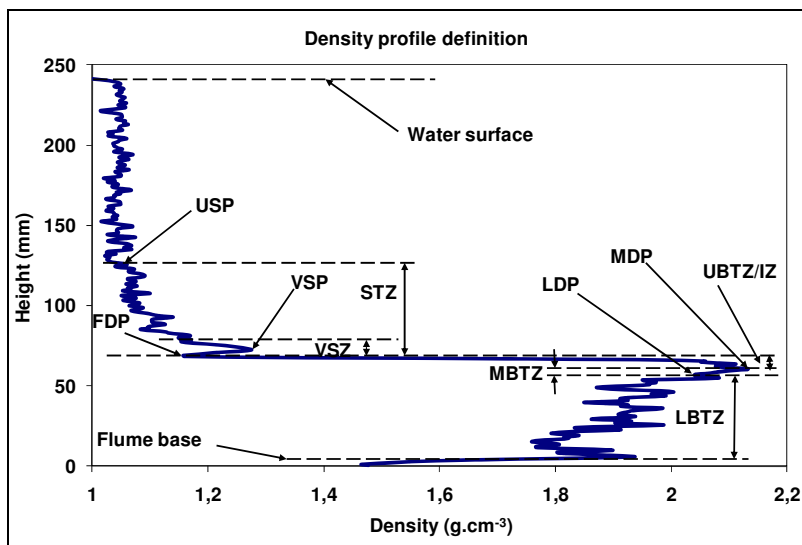


Fig. 10. Typical density profile of a sand ripple, as measured by the CT-scanner.

Starting in the upper water column, a typical curve of sediment column density encounters the upper suspension point (USP), where clear water (washload) is distinguished from suspended load by the latter's higher density (above $1.05 \text{ g}\cdot\text{cm}^{-3}$; Fig. 10). The upper suspension point may be at the water surface if turbulent flow has generated a high sediment transport rate.

The suspended transport zone (STZ) contains a significant amount of suspended sediment and may include a viscous sublayer.

The point separating the suspended load and the bedload is the frontier density point (FDP). This point is used as a reference concentration, but is not synonymous with the ripple

surface. Instead, it is at the maximum density point (MDP) at the base of the suspended zone, as defined later in the text.

The suspended transport zone includes the viscous sublayer zone (VSZ) (section 3.2), which is defined by its low density, high viscosity, and obvious distinction from the bedform. The viscous sublayer zone contains a viscous sublayer point, defined as the point of highest density and viscosity. When a viscous sublayer zone is present, the viscous sublayer point (VSP) can be used as a reference concentration instead of the frontier density point. The upper bedload transport zone (UBTZ) is delimited by the frontier density point at the top and the maximum density point at its base. Sediment in the upper bedload transport zone moves as a thin lower-density layer around low density points, and is characterized at its base by the maximum density point, an abnormally high-density point at which hydraulic pressure is linked to bed density. The maximum density point is the top of the bed *sensu stricto* and is the upper limit of shear stress lamination of the inner bed. Evolution of the maximum density point affects the lee-side avalanching process and stoss-side erosion because of fluid-related effects.

Below the maximum density point is a lower density point (LDP), characterized by water-rich sediment (less compaction) in which fluid pressure favors sediment mobility. The lower density point forms part of the inner bed shear stress lamination structure (Madsen and Durham, 2007).

Below the upper bedload transport zone is the middle bedload transport zone (MBTZ), with an upper limit at the maximum density point and a lower boundary at the lower density point. The middle bedload transport zone and upper bedload transport zone move on the low-density layer that forms around the lower density point.

Within the upper bedload transport zone is an inflection zone (IZ) that increases the thickness of the upper bedload transport zone across a hinge point or inflection density point close to the maximum density point. The inflection zone is due to lee-side avalanching and to water penetration caused by vortices located over the ripple unpacking section.

The last transport zone, the lower bedload transport zone (LBTZ) consists of a succession of layers (Wheatcroft, 2002) that move under fluid pressure induced deep in the bed (Madsen and Durham, 2007), and by an inner bedload shear stress, which causes high-density sheet sliding on low-density layers produced by water-filled porosity.

3.2 New definitions and locations of boundary layers

Bridge and Demicco (2008) explained attributes of the boundary layer using a solid ripple surface. In the present study, however, measurements show that upper bedload transport zone thickness and bedload density variation indicate pseudo-liquefaction and water ejection along part of the ripple (Figs. 21 and 22 (section 5.4)).

Water penetration through the boundary requires that the *y*-axis be modified such that motion below the boundary is included (Madsen and Durham, 2007); this also demands a different definition of the viscous sublayer environment.

Based on the sedimentological architecture previously defined in section 3.1, the upper bedload transport zone thickness is compared with the maximum density point forming the bedload *sensu stricto*. The results (Fig. 11) indicate low-density erosion (1.75 to 2.25 g•cm⁻³) for 8 to 12 mm of thickness, where the water penetrates deeply into the bedform (Montreuil and Long, 2011a). This transportation, on the upper part of the ripple's stoss-side, is near the surface (4 to 8 mm) and is characterized by higher density (2.00 to 2.25 g•cm⁻³) where and when the water leaves the bedform.

On the lee side of ripples, results indicate phase recovery of the water rather than deposition. Within the sediment column, which is 4 to 14 mm thick depending on location, density was 2.00 to 2.35 $\text{g}\cdot\text{cm}^{-3}$ with an average of 2.20 $\text{g}\cdot\text{cm}^{-3}$, indicating expulsion of water.

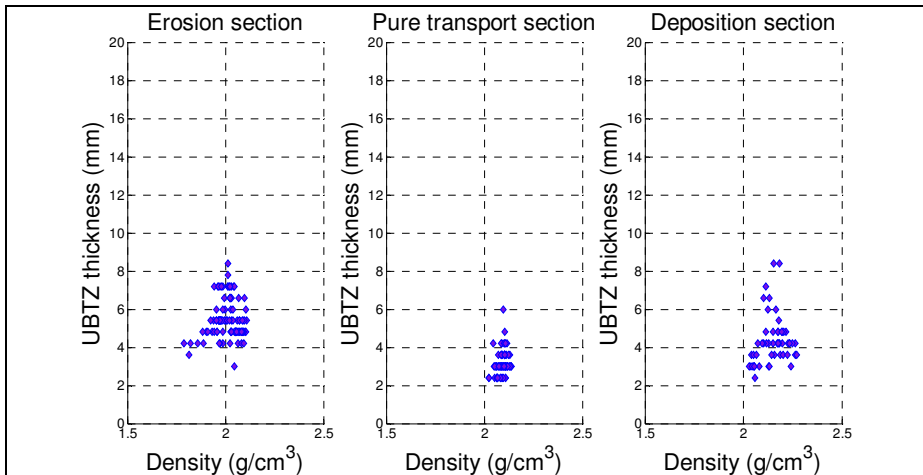


Fig. 11. Upper bedload transport zone (UBTZ) thickness as a function of the maximum density point (MDP) value, for three ripples.

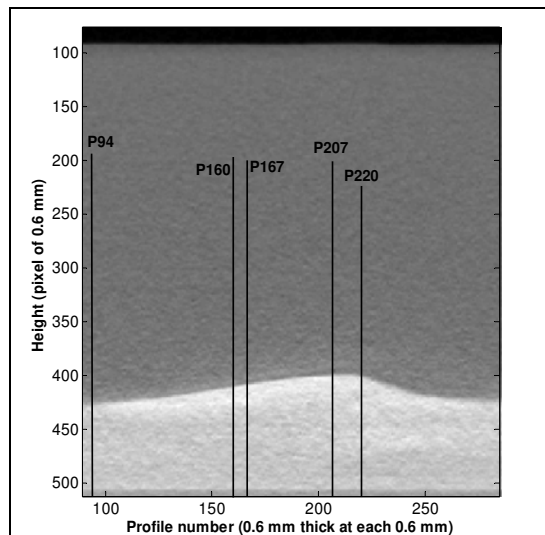


Fig. 12. X-ray image of the sand ripple (2008-No27-G), pixel size: 0.6 mm, d_{50} : 124 μm , and flow: 19 $\text{cm}\cdot\text{s}^{-1}$. The partial gray-scale density image measured using the global volume technique provides a general view for 195 of the 512 density profiles (P94 is the 94th of 512 profiles).

4. Influence of flow on the vertical density profile definition along the ripple length.

4.1 Hydraulic effect on the density profile

Hydraulic phenomena over sand ripples govern the density profiles of sediment-water mixtures (Fig. 12). Measurements were conducted using the global volume technique to obtain a pseudo-instantaneous image.

An upper suspension point with density above $1.05 \text{ g}\cdot\text{cm}^{-3}$ indicates washload in the water column or suspended load in the suspended transport zone (Fig. 10). The difference between the upper suspension zone and the frontier density point gives the suspended load height, the concentration, and the viscosity profile measured by the CT-scanner in each voxel. The frontier density point, located near the ripple surface, is the boundary between bedload and suspended load and has a density between 1.05 and $1.18 \text{ g}\cdot\text{cm}^{-3}$ depending on the sediment suspension, vortices, separation point, and re-attachment point. This point is used as a reference elevation for concentration when the viscous sublayer is absent.

4.1.1 Effect on the stoss side

Density profile P220 (Fig. 13) shows a vortex 18.4 mm in diameter. The size of this vortex in subsequent profiles indicates its shape, located between 69.5 and 87.9 mm in the turbulent section. In the turbulent section, a second suspended transport zone is present, indicating continuous transport.

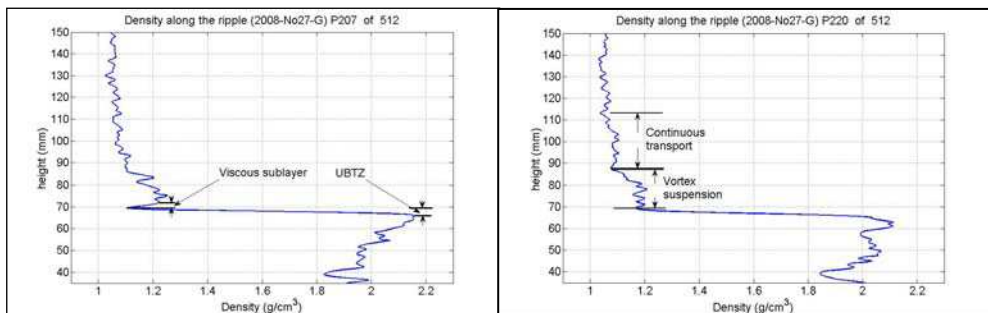


Fig. 13. Sand ripple density profile P207 shows a viscous sublayer, and density profile P220 indicates continuous transport above a vortex. (GVT; ripple ID: 2008-No27-G).

The presence of an inflection density point high on the stoss side (Fig. 13, P207-P220) indicates the presence of a saturated sediment layer that is part of the upper bedload transport zone. The maximum density point of 2.0 to $2.3 \text{ g}\cdot\text{cm}^{-3}$ is generated by hydraulic pressure near the surface on the lower part of the stoss side; its location is deeper within the sediment with increased height on the ripple and along the lee side of the ripple. The maximum density point indicates the point of traction within an area of minimum saturation.

Profile P94 (Fig. 14) indicates the absence of a viscous sublayer and the concentration of suspended sediment (Fig. 14, left). Separation section profiles are near the brinkpoint in association with the fluid separation point (Fig. 13).

Density profiles (Fig. 15, left) present the transition between a fully developed vortex and a viscous sublayer higher on the stoss side (Fig. 15, right) (Allen, 1982). The appearance of a

viscous sublayer (Fig. 15, right) indicates re-attachment of the fluid (Fig. 8). The location of this point is influenced by current velocity and the shape of the sand ripple.

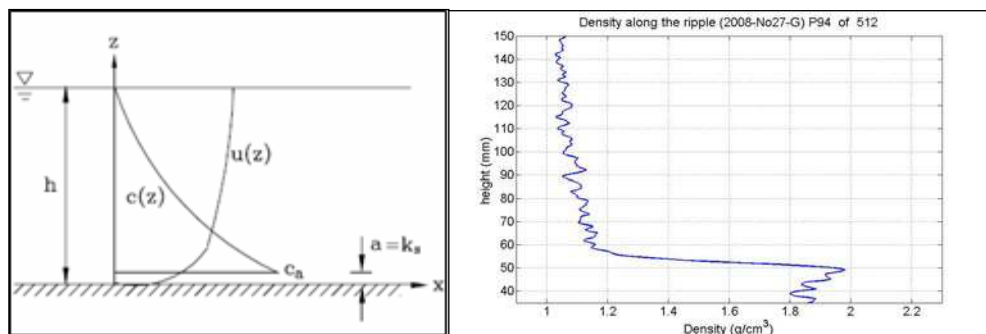


Fig. 14. Concentration and velocity profile after Liu (2001), and sand ripple density profile P94, presenting a classical log concentration profile. (GVT; ripple ID: 2008-No27-G).

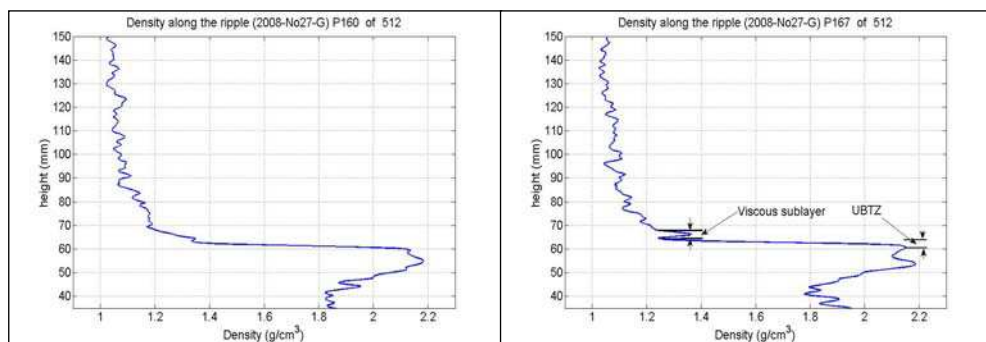


Fig. 15. Sand ripple density profiles P160 and P167, including the transition from a vortical section to a fully developed viscous sublayer and associated water ejection. (GVT; ripple ID: 2008-No27-G).

On profile P167 (Fig. 15, right), the viscous sublayer zone and upper bedload transport zone are about 1.8 mm and 3.6 mm thick, respectively. The viscous sublayer is thinner than the upper bedload transport zone, but its water-sediment density variations are different, ranging from 1.37 to 1.24 $\text{g}\cdot\text{cm}^{-3}$ for the viscous sublayer zone and 2.15 to 1.24 $\text{g}\cdot\text{cm}^{-3}$ for the upper bedload transport zone, indicating mainly suspended transport due to fluid pressure and velocity influencing the bedload erodibility.

Comparison of density profiles P207 and P220 (Fig. 13) indicates modification of fluid behavior representing a separation position over the ripple. Profile P207 shows a viscous sublayer, but profile P220 does not (Fig. 13). Density at the frontier density point retreats near the water density ($1.024 \text{ g}\cdot\text{cm}^{-3}$) and becomes $1.168 \text{ g}\cdot\text{cm}^{-3}$. This thin layer (Fig. 13, left) represents a viscous sublayer between the suspended transport zone, whereas the upper bedload transport zone represents a thicker layer containing vortical perturbations that affect the lee sides of the ripples (Fig. 13, right).

4.1.2 Effect on the lee side

From the ripple crest to the top of the lee side, the thickness of the upper bedload transport zone increases from 6.5 to 13.7 mm, a change that is linked to the avalanching process (Fig. 13, P220). Density regression of the lower density point indicates the upper erosion limit of the previous foreset on the stoss side and deposition on the lee side. The presence of an inflection density point on the lee side (Fig. 10, P94) shows the presence of a saturated layer caused by avalanching. On the lee side, density changes from 2.3 to 1.9 $\text{g}\cdot\text{cm}^{-3}$.

4.2 Thickness variation in sand ripple transport zones

Each of the transport zones presented in section 3.1 has its own characteristic thickness and evolution. These typical characteristics are described below, beginning in the water column (Fig. 16).

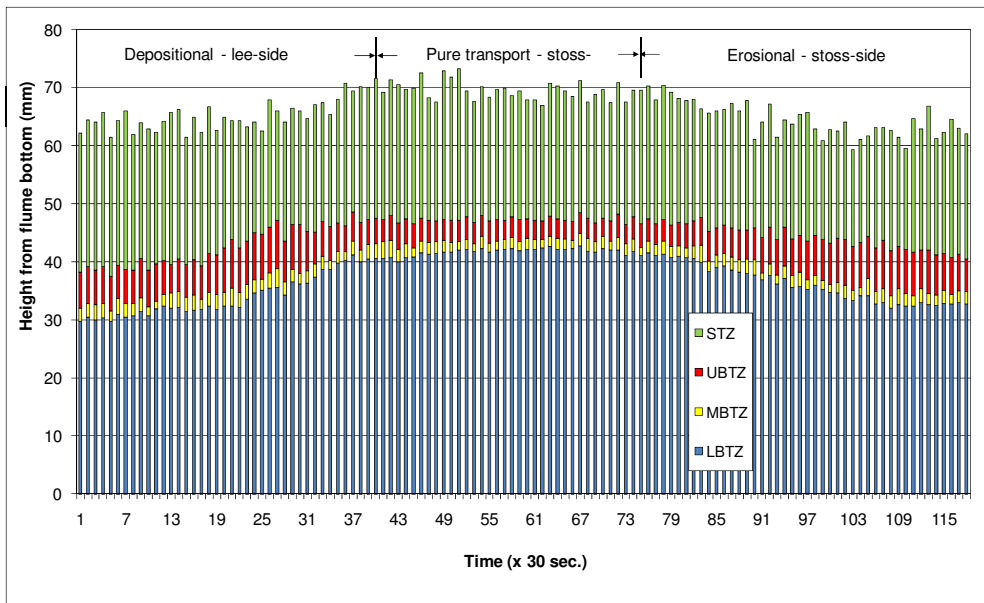


Fig. 16. Composition of the sand ripple transport zone. (PSVT; ripple ID: 2010-No5-C).

The suspended transport zone thickness along the ripple remains relatively stable at 21 mm, when the upper suspension point is chosen at 1.18 $\text{g}\cdot\text{cm}^{-3}$. Below the suspended transport zone, the upper bedload transport zone is at about 6.1 mm on the lee side. This thicker zone is associated with an inflection zone correlated with a thicker middle bedload transport zone (approximately 3 mm). Inside the upper bedload transport zone, the shear-stress decreases vertically in inverse proportion to the water concentration, which governs the viscosity and consequently the degree of sediment transport or deposition.

In the pure transport area on the stoss side (Montreuil and Long, 2011a), the middle bedload transport zone and upper bedload transport zone are thinner (2 and 4 mm, respectively). These thicknesses indicate a weak fluid influence due to protection by the viscous sublayer zone.

During erosion under vortical action, thickness of the upper bedload transport zone reaches 10 mm, and that of the middle bedload transport zone is 2 mm, with a standard deviation of 2 mm. These values are caused by strong vortices active on the lower stoss side and by micro-turbulence around the reattachment point. The transport zone thickness varies along the ripple as a function of hydrodynamic variations, indicating that variable compaction is taking place deep in the ripple interior.

5. Bedload density parameters and their relation to hydrodynamics.

5.1 Effect over the lower stoss-side section

In erosional areas P90 to P160 and P150 to P180 (Fig. 17), vortex pressure causes an augmentation of suspension just above the bedload and a reduction of density, or liquefaction, which helps the sediment unpack, resulting in suspended load. When leaving the erosional section (P140), as compared to the previous profile (P150), the slope of the upper bedload transport zone transition approaches the horizontal, indicating an absence of sediment passing from bedload to suspended load. Profile P140 is approximately in a pure transport section.

In the part of the vortex in which the current is directed downward, the suspended sediment concentration is low. Sediment concentration increases in the lower, horizontal part of the vortex, between the downward and upward movement. The highest sediment concentration is in the part of the vortex where water movement is upward (Montreuil and Long, 2011a).

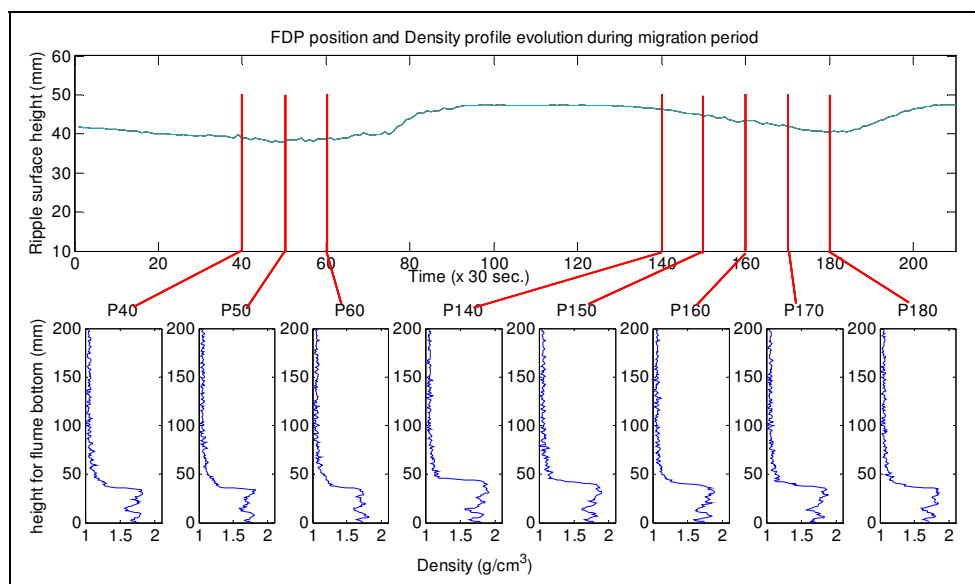


Fig. 17. Frontier density point, upper part of upper bedload transport zone (above), and sand ripple density profiles measured with periodic single volume technique (below). Profiles P40 to P60 and P140 to P180 are located in the erosional section of the lower stoss side. (PSVT; ripple ID: 2010-No5-C).

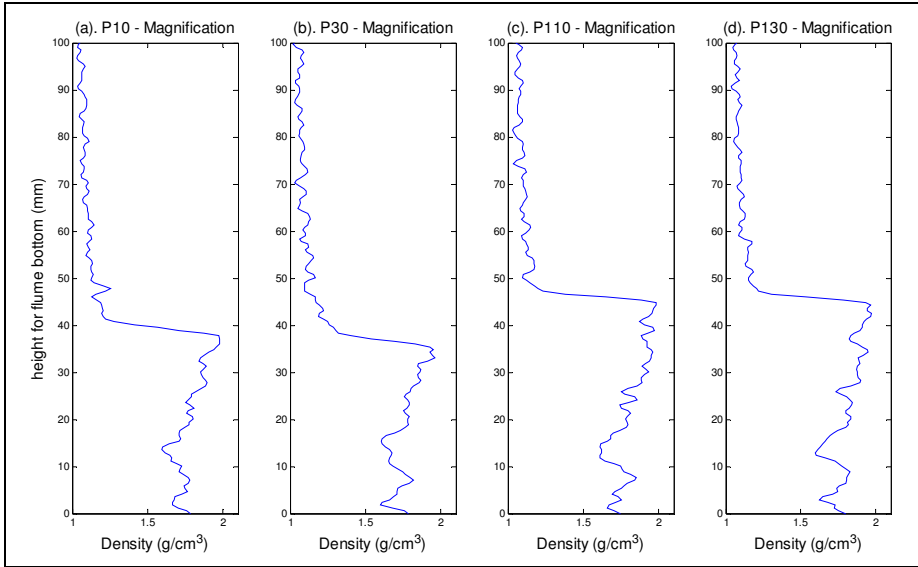


Fig. 18. Magnification of density profiles P10 (viscous sublayer section), P30 (vortex section), P110 (pure transport section with viscous sublayer), and P130 (between vortex and viscous sublayer section). (PSVT; ripple ID: 2010-No5-C).

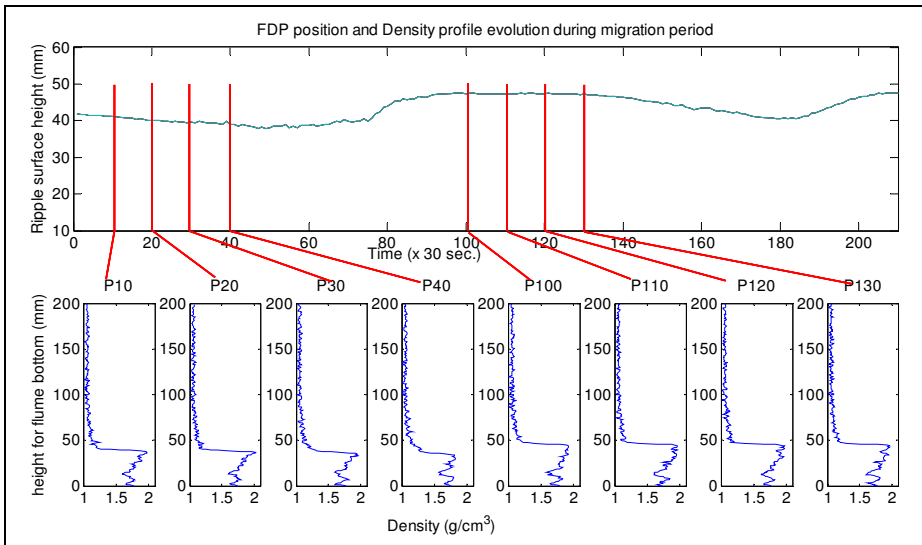


Fig. 19. Frontier density point and upper part of the upper bedload transport zone (above) and sand ripple density profiles measured with the periodic single volume technique (below). Profiles P10 to P40 are located in the erosional section (middle stoss side) and profiles P100 to P130 are located in the pure transport section (upper stoss side). (PSVT; ripple ID: 2010-No5-C).

5.2 Effect over the upper stoss-side section

The transition from erosional profile P40 (Fig. 18) to pure transport profile P10 (Fig. 19) is marked by density variation in the upper bedload transport zone ($0.56 \text{ g}\cdot\text{cm}^{-3}$ at P40 to $0.78 \text{ g}\cdot\text{cm}^{-3}$ at P10). This increased upper bedload transport zone density transition, indicated by a frontier density point reduction ($0.06 \text{ g}\cdot\text{cm}^{-3}$) and a maximum density point increase ($0.16 \text{ g}\cdot\text{cm}^{-3}$), signifies a reduction in liquefaction, followed by unpacking. This transition corresponds to the disappearance of the vortex and change to a pure transport section with a thin upper bedload transport zone. Profiles P100 (4.72 mm) to P130 (8.26 mm) contain a viscous sublayer zone (Fig. 19, P110) and a maximum density point that decreases from 1.97 to $1.93 \text{ g}\cdot\text{cm}^{-3}$ as fluid pressure is decreased.

5.3 Effect over the lee-side section

Profiles P180 to P200 (Fig. 20) confirm a density evolution that is related to avalanching, and profiles P60 to P100 depict the transition from suspended load to bedload settling. This transition is characterized by an increase in bedload density (1.73 to $1.93 \text{ g}\cdot\text{cm}^{-3}$) and decrease in reference concentration Ca (1.25 to $1.14 \text{ g}\cdot\text{cm}^{-3}$). Bedload density near the flume bottom remains roughly constant, with slight variation due to compaction.

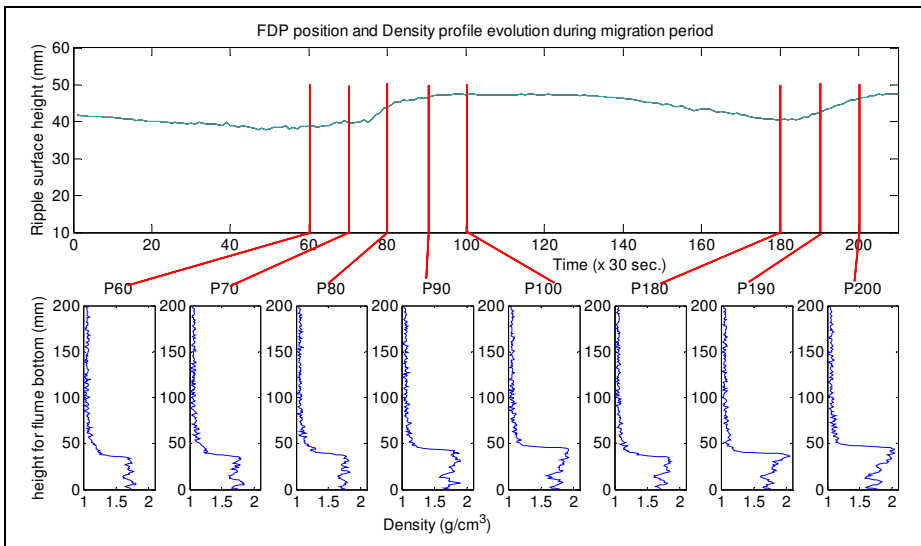


Fig. 20. Frontier density point for the upper part of the upper bedload transport zone (above) and sand ripple density profiles measured with the periodic single volume technique (below). Profiles P60 to P100 and P180 to P200 are from the depositional sides (lee sides) of ripples and record evolution of suspended load and bedload density in the lee side (PSVT; ripple ID: 2010-No5-C).

The lower part of the lee side differs from the upper part in having a lower bedload density ($1.71 \text{ g}\cdot\text{cm}^{-3}$) indicating weak compaction at the base. The upper lee side is dominated by a high frontier density point value of $1.16 \text{ g}\cdot\text{cm}^{-3}$, as compared to $1.25 \text{ g}\cdot\text{cm}^{-3}$ for the base, and has a higher maximum density point, which resulted from compaction during the 900 s (15 min) time interval that separated P60 from P90. Through this time interval (periodic single

volume technique), the internal structure of the bedload remains similar, but the bedload density value, from the base to the top, varies as a function of sediment compaction in the lower position and in response to fluid pressure near the surface. The sediment matrix is, therefore, under the influence of both phenomena.

5.4 Effect over the three main sections

The surface of a sand ripple has three main sections: an erosional section, a pure transport section, and a depositional section (Montreuil and Long, 2011a). The most important difference among those sections is water penetration depth (Fig. 21). Unlike the pure transport zone, in which the upper bedload transport zone is 5 mm thick, the erosional section has an upper bedload transport zone 12 mm thick, indicating deeper water penetration and lower viscosity, both of which favor sediment erosion and initiation of transport (Fig. 22). The density at ripple surfaces is lower ($1.85 \text{ g}\cdot\text{cm}^{-3}$) under the vortical erosional effect than it is in the pure transport zone ($1.90 \text{ g}\cdot\text{cm}^{-3}$). This difference is due to water penetration and pressure applied by surface fluid, as demonstrated by Middleton and Southard (1977).

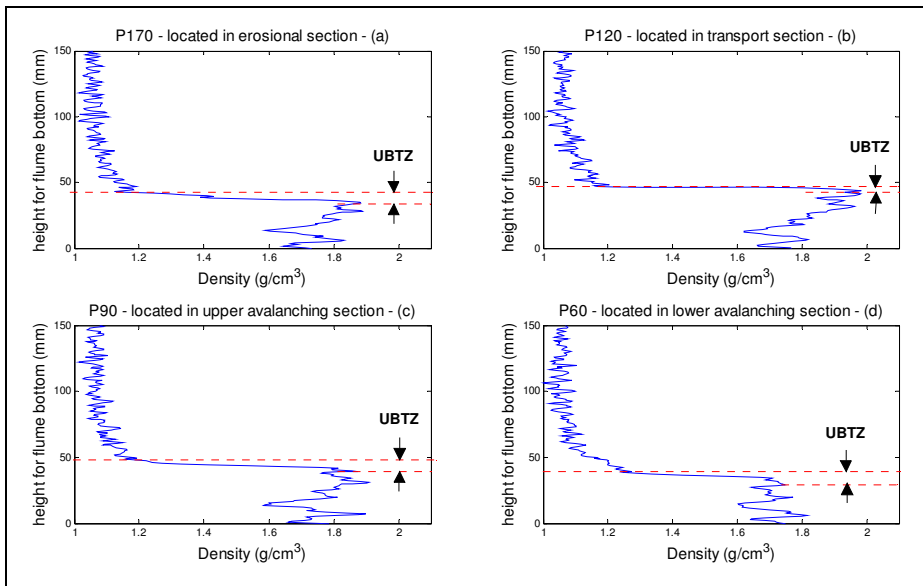


Fig. 21. Density profile of sand ripples and thickness of upper bedload transport zone in the erosional section, pure transport section, upper lee side, and lower lee side, as measured using the periodic single volume technique (PSVT; ripple ID: 2010-No5-C).

When ripples migrate, the stoss side of each ripple is covered by sediment deposited on the lee side of the next, approaching ripple. Thickness of the upper bedload transport zone decreases because of water expulsion caused by forward movement of the vortex and sediment compaction (Fig. 22). Water ejection is recorded in the density change in the upper bedload transport zone, showing a decrease from 2.06 to $1.84 \text{ g}\cdot\text{cm}^{-3}$. The maximum density point exhibits a small variation in density ($0.028 \text{ g}\cdot\text{cm}^{-3}$) between 28.32 and 41.89 mm above

the bed bottom. Deeper in the bed, in the lower bedload transport zone, subtle density variations are due to compaction and water migration.

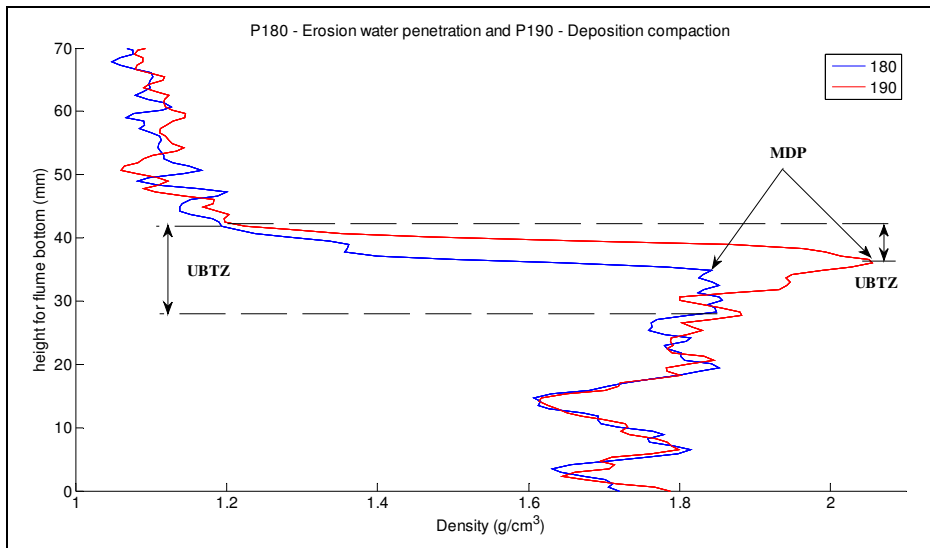


Fig. 22. Density profile P180 (blue), from the vortex section, has a high concentration caused by fluctuation in the location of the transition between the frontier density point and the maximum density point. Density profile P190 (red), from the lower lee-side avalanching section, shows an elevated maximum density point, an increased density in the middle bedload transport zone, and a similar density in the lower bedload transport zone, an area that had already been affected by migration of the sediment mass of the preceding ripple. (PSVT; ripple ID: 2010-No5-C).

Bedload transport occurs in two regimes: initial bedload mobilization and sheet-flow bedload (King, 2005). The density of the lower part of the sheet flow, just above the stationary (flat) bed, is defined by the maximum density point of the upper bedload transport zone. In this study, sheet-flow refers to the entire bedload transport zone and is used to define the boundary with suspended transport, but maximum density is located between the upper bedload transport zone and the middle bedload transport zone. The upper bedload transport zone, which rises and then collapses along the sand ripple under moving fluid, can be conceptualized as a moving sheet of material. It works well until the thickness of the layer decreases to the order of a grain diameter, at which point the viscous sublayer breaks down.

Any sediment bed has a characteristic surface roughness (Fig. 14; Liu, 2001). In this study, profiles along a ripple indicate changes in this roughness around the frontier density point and a more complex transition between suspended load and bedload. This observation emphasizes the need for CT-scanner measurements (Fig. 14) for further investigation of the transition between suspended load and bedload.

According to Bridge and Demicco (2008), viscous (surface) sublayer drag is dominant on both hydraulically smooth and hydraulically rough boundaries. Pressure (form) drag is so

strong that viscous forces can be ignored. In this study, the smooth boundary is in the pure transport zone and contains the viscous sublayer zone, which moves on a well-defined bedload with a thin upper bedload transport zone with a high density at the maximum density point. In the erosional ripple zone, which has a rough boundary, the viscous layer is replaced by a thicker upper bedload transport zone caused by a more intense and larger diameter vortex.

Bed roughness thickness is commonly considered to be equivalent to ripple height (Bijker, 1992; Liu, 2001), but in this study, concentration profiles and porosity along the ripples were not constant, and this general statement is accurate only for a macroscopic view of a small ripple (~20–30 mm long). For a ripple longer than 30 mm, bed roughness can be micro-analyzed in subsections. Such ripple micro-analysis is necessary because of the fluctuating conditions along its length. The main zones involved in bed roughness are a function of flow: suspended transport zone, viscous sublayer zone, upper bedload transport zone, and middle bedload transport zone.

6. Vortex analysis

6.1 Effect of vortex on bedload architecture of the lower stoss side

The contribution of vortices to sediment erosion is undisputed, but their effect deep inside the bedload has been unknown until now. CT-scanner imaging of ripples reveals the vortex sediment content through density profiles and the effect of vortices on the structural integrity of the bedload.

Vortices have three parts. The first (Fig. 23, P147) is where the sediment-poor fluid (lowest concentration) is dragged downward and begins to apply pressure that deepens the critical shear stress (discussed in section 6.2). The second part of the vortex is the longitudinal part of the vortex (Fig. 23, P153). This part is characterized by a higher average density in the suspended load ($1.11 \text{ g}\cdot\text{cm}^{-3}$ around 90 mm from the bottom, as opposed to $1.06 \text{ g}\cdot\text{cm}^{-3}$ for surrounding volumes). This suspended sediment is entrained by the upward rotating part of the flow (left-pointing arrow in Fig. 23, P153). The average density appears lower because of sediment expelled by centripetal force. These density values are not entirely accurate, however, because the X-ray integration of stationary rotating sediment overestimates the value, but the relative values remain significant. At the bottom of the vortex, flow is inverted (right-pointing arrow). This backward flow initiates sediment unpacking, causing the thickness of the upper bedload transport zone to increase to 8.85 mm, and conditioning the sediment to leave the bedload. The density transition from the frontier density point to the maximum density point is disturbed by this pseudo-liquefaction. A maximum density point forms ~35 mm from the bottom (Fig. 23, P153). This deep point indicates the formation of a temporary ripple surface *sensu stricto*, due to the fluid velocity trying to move the bedform backward. The ripple surface resists backward motion by increasing shear stress, causing more friction among grains.

The third part of the vortex is its upward motion. In this area, the deep pressure of the second vortex zone is released. Sediment in the upper bedload transport zone is waterlogged and has minimal intra-granular friction. The sediment leaves the bedload as water previously contained in the bedload matrix is released. Density profile P162 (Fig. 23) shows an average suspended sediment concentration (equation 2) of 0.56, which contrasts with the values of 0.53 and 0.54 for P147 and P153, respectively.

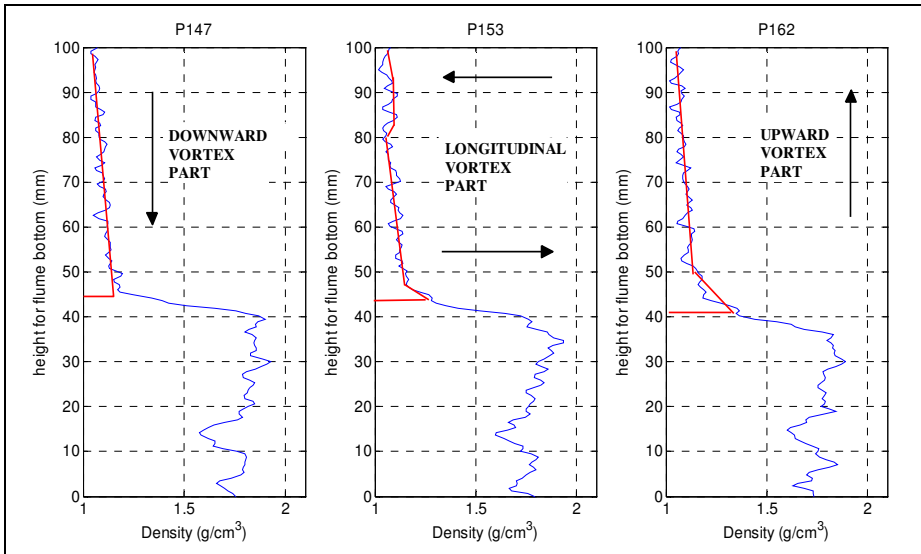


Fig. 23. Density profiles measured in three parts of a stoss-side vortex. Profile P147 is in the downward-moving part of the vortex, P153 is located in the longitudinal part, and P162 is located in the upward part.

This increased concentration originates from sediment liquefaction and uplifting. The last influence of the upward-moving part of the vortex is marked by the elevation of the maximum density point, which rebuilds a higher ripple surface *sensu stricto*. The maximum density point passes from $1.78 \text{ g}\cdot\text{cm}^{-3}$ in P153 to $1.83 \text{ g}\cdot\text{cm}^{-3}$ in P162, producing a surface elevation of $\sim 2\text{--}4 \text{ mm}$.

The vortex is characterized in general by an average maximum density point density of approximately $1.83 \text{ g}\cdot\text{cm}^{-3}$, in contrast to $2.04 \text{ g}\cdot\text{cm}^{-3}$ outside the vortex part of the ripple. In the upper bedload transport zone, the transition from the frontier density point to the maximum density point is thick, but, unlike the lee-side avalanche transition zone, it is neither continuous nor smooth. It is perturbed by the turbulence surrounding the vortex.

6.2 Shear stress effect on bedload architecture

The shear stress in a viscous fluid composed of water and sediment and moving along a solid boundary induces the shear stress on the boundary (Yalin, 1992). The no-slip condition dictates that the speed of the fluid at the boundary (relative to that boundary) is zero but, at some height from the boundary, the flow speed must increase to equal the fluid speed. The region between these two points is aptly named the boundary layer. Shear stress is produced in this boundary layer as a result of this difference in velocity and can be expressed as

$$\tau_w = \mu \frac{\partial u}{\partial y} \quad (7)$$

where μ is the dynamic viscosity of the fluid, u is the velocity of the fluid along the boundary, and y is the thickness of the boundary layer. As demonstrated in section 4, the

sand ripple bedload (more specifically the upper bedload transport zone) is not a solid boundary, and the dynamic viscosity of the fluid μ is replaced by the viscosity of the inner bedload μ_i , which pushes the no-slip condition deep into the bed. The boundary thickness is now taken from the real ripple surface, which corresponds to the maximum density point, located at the lowest point in the upper bedload transport zone (Fig. 24).

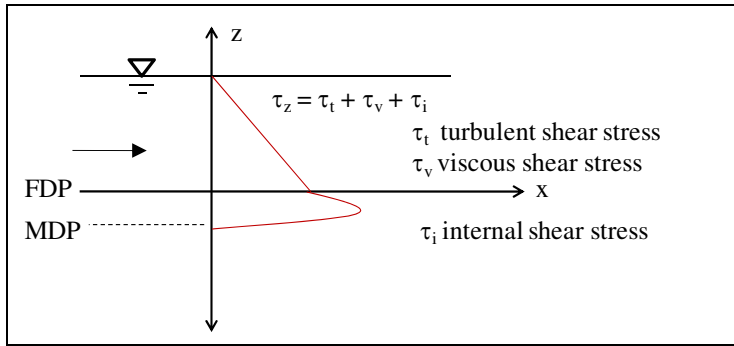


Fig. 24. New shear stress definition, which includes water penetrating into the sediment and increasing the depth at which sediment transport is initiated.

7. Conclusions

Computed axial tomography (CT-scanning) is a non-destructive technique for generating images that map the numerical density of a sand-water mixture. The data produced depict the evolution of sedimentological parameters by variation in density, concentration, porosity, and viscosity of the water-sediment mixture. Results can be obtained for every section of a ripple, using zones and inflection points in density patterns. These transport zones evolve longitudinally in the form of layers that vary in their properties along the length of each ripple.

This study demonstrates that understanding of the hydraulic phenomena behind sediment transport can be improved by reference to density points and zones. The value of CT-scanning lies in its ability to provide numerical parameters associated with the sediment-water interface and with features associated with shear stress deep inside the bed. CT-imaging highlights the importance of water penetration deep into the erosional area on the stoss side of ripples. Accurate measurements of the viscous sublayer reveal the intimate connection between suspended load and bedload. Density measurements of the lee sides of ripples highlight compaction phenomena associated with water ejection.

The density profile of a sand ripple consists of the upper bedload transport zone, the middle bedload transport zone, and the lower bedload transport zone, which form successive layers that shear against each other. These bedload transport layers move on a thin, low-density layer that forms at the low-density point. As indicated by Raudkivi (1963), Vanoni and Hwang (1967), and Middleton and Southard (1977), hydraulic pressure over the bed induces slow motion deep inside the bed (Madsen and Durham, 2007). The horizontal pressure gradient persists deep inside the bed, creating a deep shear stress that produces a laminated transport layer between the lower density point and a higher density layer (maximum density point). Thicknesses of these layers have been correlated to sediment grain size

(Montreuil and Long, 2011b), but the velocity of particles within the bed has not been quantified.

The viscous sublayer exists only in the middle of the ripple stoss side, down-flow from the fluid reattachment point, where interstitial water is ejected from the sediment. The viscous sublayer is absent in locations where vortices erode the ripple and where the sediment is deposited on the lee sides (avalanche face) of ripples.

Stoss-side laminae contain two zones, the upper bedload transport zone and the middle bedload transport zone (Reineck and Singh, 1975). The static foreset laminae, at the bottom of the stoss side, form the lower bedload transport zone.

This study confirms the existence and location of major hydraulic points and zones under various environments, and also reveals new parameters related to flow and sediment properties. The results also provide a new shear stress profile that includes activity deep inside the bedform, particularly in areas affected by vortices. Pervasive small-scale variability is present in the density of near-surface sands, which may have important implications for the measurement of sediment transport using high-frequency acoustics.

Related work, already in progress, will include an exhaustive analysis of velocity and grain-size effects on the dynamics of sedimentological parameters. The link between shear stress within the bed and the upper bedload transport zone will be examined. Bed motion was not covered in this study but will be measured using X-ray sediment tracking.

8. Acknowledgments

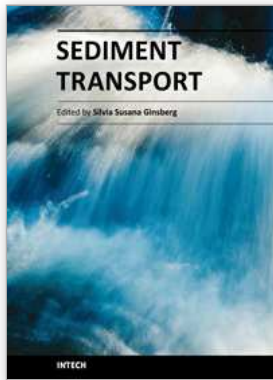
Special acknowledgment to the Canadian Foundation for Innovation (CFI) and the GEOIDE project for their financial contributions and to L. F. Daigle and M. Des Roches for technical support and work.

9. References

- Allen, J.R.L. (1968). *Current Ripples: Their Relation to Patterns of Water and Sediment Motion*. Amsterdam, North-Holland.
- Allen, J.R.L. (1982). *Sedimentary Structures: Their Character and Physical Basis* (Two volumes) Elsevier, New York, 593 p. (v. 1) and 663 p. (v. 2).
- Allen, J.R.L. (1984). *Sedimentary Structures-Their Character and Physical Basis*. Elsevier Publishers, Amsterdam, 1256 pp.
- Allen, G.P. and Posamentier, H.W. (1994). Transgressive facies and sequence architecture in mixed tide- and wave-dominated incised valleys: example from the Gironde estuary, France. In: Dalrymple, R. W., Zaitlin, B. A. & Boyd, R. (eds.) *Incised valley systems: origin and sedimentary sequences*, Society of Economic Paleontologists and Mineralogists, Special Publications, 51, 225-240.
- Bennett, S.J. and Best, J.L. (1995). Mean flow and turbulence structure over fixed, two-dimensional dunes: implication for sediment transport and dune stability. *Sedimentology* 42, 491-514
- Bijker E.W. (1992). Mechanics of sediment transport by the combination of waves and current, *23rd Int. Conf. on Coastal Engineering*, Venice, 147-173.
- Bridge J.S. (2003) *Rivers and Floodplains: Forms, Processes, and Sedimentary Record*. Oxford: Blackwell.

- Bridge J. and Demicco R. (2008). *Earth Surface Processes, Landforms and Sediment Deposits*. Cambridge University Press, New York, 830pp.
- Brown, R. (1828). A brief account of microscopical observations made in the months of June, July and August, 1827, on the particles contained in the pollen of plants; and on the general existence of active molecules in organic and inorganic bodies, *Phil. Mag.* 4, 161-173.
- Carmenen B. and Larson M. (2004). A general formula for non-cohesive bed load sediment transport, *Estuarine, Coastal and Shelf Science* 63 (2005) 249–260.
- Duchesne, M. J., Long, B. F., Labrie, J., and Simpkin, P. G. (2006). On the use of computerized tomography scan analysis to determine the genesis of very high resolution seismic reflection facies, *J. Geophys. Res.*, 111, B10103, doi: 10.1029/2006JB004279.
- Duliu, O.G. (1999). Computer axial tomography in geosciences: an overview. *Earth-Science Reviews* 48, 265–281.
- Kak A. C. and Slaney M. (1999). *Principles of computerized tomographic imaging*, IEEE PRESS, New York, 329 pp.
- Kastaschuk R. and Villard P. (2001). *Turbulent sand suspension over dunes*. *Fluvial Sedimentology VI*. Blackwell Science. 478pp.
- Ketcham R.A. and Carlson W.D. (2001). Acquisition, optimization and interpretation of X-ray computed tomographic imagery: applications to the geosciences, *Computers & Geosciences* 27 (2001) p.381– 400.
- King D. B. Jr. (2005). Influence of grain size on sediment transport rates with emphasis on the total longshore rate, *US Army Corps of Engineers, ERDC/CHL CHETN-II-48*, 24pp
- Langhorne, D. N. (1981) An evaluation of Bagnold's dimensionless coefficient of proportionality using measurements of sandwave movement. (*Mar. Geol.*) 43: 49-64.
- Liu Z. (2001). *Sediment transport, Laboratoriet for Hydraulik og Havnebygning, Institutet for Vand, Jord og Miljøteknik*. Aalborg Universitet 71 pp.
- Madsen, O.S. and Durham, W.M. (2007). Pressure-Induced subsurface sediment transport in the surf zone. *Proceedings Coastal Sediments '07 Conference, ASCE, New Orleans, LA*, 1:82-95.
- McLean, S. R. (1983). *Turbulence and sediment transport measurements in a North Sea tidal inlet (The Jade)*. In *North Sea Dynamics*, ed. J. Sundermann, W. Lang, pp. 436-52. Berlin: Springer-Verlag.
- Mees, F. Swennen, R. Van Geet, M. and Jacobs, P. (2003). Applications of X-ray computed Tomography in the Geosciences. *Geological Society of London Special Publication* 215.
- Middleton G.V. and Southard J. B.; (1977). *Mechanics of sediment movement*, S.E.P.M. Short Course Number 3, Binghamton.
- Montreuil S. (2006). *Évolution dimensionnelle des structures de rides en déplacement sous un courant stationnaire mesuré sous scanographe dans un canal en boucle verticale*. MSc Thesis, INRS-ETE, Québec. 121 pp., (unpub.).
- Montreuil S. and Long B. (2007). Flume experiments under CAT-scan to measure internal sedimentological parameters during sediment transport, *Proceedings Coastal Sediments '07 Conference, ASCE, New Orleans, LA*, 1:124-136.
- Montreuil S. and Long B. (2011a). Relationship between vortex activity and pseudo liquefaction at a lower stoss-side ripple surface, *Proceedings Coastal Sediments '11 Conference, ASCE*, in press.

- Montreuil S. and Long B. (2011b). CT-scanner measurement of sand ripple sedimentological parameters, a definition. *Sedimentology*, In Prep.
- Moore, F. 2004, *Application de la scanographie à l'étude de la déposition consolidation: Modélisation physique et théorique*, M.S. thesis, 131 pp., Inst. Nat. de la Rech. Sci., Centre Eau, Terre, Environ., Québec.
- Nummedal, D., Riley, G. W. and Templet, P. L. (1993). High-resolution sequence architecture: a chronostratigraphic model based on equilibrium profile studies. In: Posamentier, H. W., Summerhayes, C. P., Haq, B. U. & Allen, G. P. (eds.) *Sequence Stratigraphy and Facies Associations, International Association of Sedimentologists, Special Publications*, 18, 55–68.
- Raudkivi, A. J. (1963). Study of sediment ripple formation. *ASCE J. Hydraul. Div.*, 89, 15-33.
- Reineck H.-E. and Singh I.B. (1975). *Depositional Sedimentary Environments*, Springer study edition, New York, 439 pp.
- Schneider, U., Pedroni, E. and Lomax, A. (1996). The calibration of CT Hounsfield units for radiotherapy treatment planning, *Phys. Med. Biol.* 41 (1996) 111–124.
- Sternberg, R. W. (1967). Measurements of sediment movement and ripple migration in a shallow marine environment. *Mar. Geol.* 5:195-205.
- Teeter Allen M. and Pankow Walter (1989). *Deposition and erosion testing on the composite dredged material sediment sample from New Bedford harbour, Massachusetts*, Technical report HL-89-11, US Army Corps of Engineers, Washington, 61 pp.
- Tucker M.E. (2001). *Sedimentary petrology* 3ed. Blackwell Science. 262pp.
- Vanoni, V. A. and Hwang, L. S. (1967) Relation between bedforms and friction in streams. (Journal of the Hydraulics Division), ASCE, Vol. 93, No. HY3, pp. 121-144.
- Van Wagoner, J. C. 1995. Sequence stratigraphy and marine to non-marine facies architecture of foreland basin strata, Book Cliffs, Utah, U.S.A. In: Van Wagoner, J. C. and Bertram, G. T. (eds.) *Sequence Stratigraphy of Foreland Basin Deposits, American Association of Petroleum Geologists Memoir*, 64, 137–223.
- Wheatcroft R.A. (2002). In Situ Measurements of Near-Surface Porosity in Shallow-Water Marine Sands. *IEEE Journal of Oceanic Engineering*, vol. 27, no. 3, pp. 561–570.
- Wilkinson, R. H., Moore, E. J., Salkield, A. P. (1985). Photogrammetry in sediment transport studies. In: *Underwater Photography and Television for Scientists*, ed. J. D. George, G. I. Lythgoe, J. N. Lythgoe, pp. 109-21. Oxford: Clarendon. 184 pp.
- Yalin, M.S. (1977). *Mechanics of Sediment Transport. (2nd edition)* Pergamon Press, Oxford, 298 pp.
- Yalin, M.S. (1992). *River Mechanics*. Pergamon Press, Oxford, 219 pp.



Sediment Transport

Edited by Dr. Silvia Susana Ginsberg

ISBN 978-953-307-189-3

Hard cover, 334 pages

Publisher InTech

Published online 26, April, 2011

Published in print edition April, 2011

Sediment transport is a book that covers a wide variety of subject matters. It combines the personal and professional experience of the authors on solid particles transport and related problems, whose expertise is focused in aqueous systems and in laboratory flumes. This includes a series of chapters on hydrodynamics and their relationship with sediment transport and morphological development. The different contributions deal with issues such as the sediment transport modeling; sediment dynamics in stream confluence or river diversion, in meandering channels, at interconnected tidal channels system; changes in sediment transport under fine materials, cohesive materials and ice cover; environmental remediation of contaminated fine sediments. This is an invaluable interdisciplinary textbook and an important contribution to the sediment transport field. I strongly recommend this textbook to those in charge of conducting research on engineering issues or wishing to deal with equally important scientific problems.

How to reference

In order to correctly reference this scholarly work, feel free to copy and paste the following:

Long Bernard and Montreuil Stéphane (2011). Evolution of Ripple Field Architecture during Sediment Transport, as Measured by CT Scanning, *Sediment Transport*, Dr. Silvia Susana Ginsberg (Ed.), ISBN: 978-953-307-189-3, InTech, Available from: <http://www.intechopen.com/books/sediment-transport/evolution-of-ripple-field-architecture-during-sediment-transport-as-measured-by-ct-scanning>

INTECH

open science | open minds

InTech Europe

University Campus STeP Ri
Slavka Krautzeka 83/A
51000 Rijeka, Croatia
Phone: +385 (51) 770 447
Fax: +385 (51) 686 166
www.intechopen.com

InTech China

Unit 405, Office Block, Hotel Equatorial Shanghai
No.65, Yan An Road (West), Shanghai, 200040, China
中国上海市延安西路65号上海国际贵都大饭店办公楼405单元
Phone: +86-21-62489820
Fax: +86-21-62489821

© 2011 The Author(s). Licensee IntechOpen. This chapter is distributed under the terms of the [Creative Commons Attribution-NonCommercial-ShareAlike-3.0 License](#), which permits use, distribution and reproduction for non-commercial purposes, provided the original is properly cited and derivative works building on this content are distributed under the same license.